Doreau-Malioche, J. *et al.* (2019) ***Géotechnique Letters* 00**, 1–9, https://doi.org/10.1680/jgele.18.00232

Characterising processes at sand-pile interface using digital image analysis and X-ray CT

J. DOREAU-MALIOCHE*, A. GALVIS-CASTRO†, R. TOVAR-VALENCIA‡, G. VIGGIANI*, G. COMBE*, M. PREZZI† and R. SALGADO†

This paper presents the results of a tensile and a compressive load tests on an instrumented model pile pre-installed in medium–dense sand samples prepared in a half-circular calibration chamber with viewing windows along its symmetry plane. Digital image correlation (DIC) is used to obtain the displacement and strain fields in the sand surrounding the pile during and after loading. The orientation of the principal strains in the soil in the vicinity of the pile depends on the loading direction. To complement the description of sand-pile interface provided by DIC, a study is conducted at a smaller scale for the analysis of intergranular contacts. After loading, resin-cemented specimens are recovered from the vicinity of the pile and investigated at the grain scale by means of X-ray computed tomography. Novel qualitative results show the spatial evolution of contacts orientations for both tests. The two advanced image-based techniques used in this study give access to valuable micro-scale information and could be combined to better understand the deformation mechanisms driving the macroscopic response of non-displacement piles.

KEYWORDS: piles & piling; strain

NOTATION

B	diameter of the model pile
C_u	coefficient of uniformity
C_c	coefficient of curvature
D_{50}	mean particle size of soil
D_R	relative density
d_c	interface critical-state friction angle for the sand-pile interface
E_1	major principal component of Green-St. Venant strain tensor in *r-z* plane
E_2	minor principal component of Green-St. Venant strain tensor in *r-z* plane
e_{max}	maximum void ratio
e_{min}	minimum void ratio
G_s	specific gravity of soil
$q_{s,avg}$	average unit shaft resistance
q_{sL}	limit unit shaft resistance
q_{sP}	peak unit shaft resistance
R_{max}	maximum roughness
R_n	normalised surface roughness
r_p	radius of model pile
r	radial distance from soil element to centreline of model pile
u	radial displacement of soil element
v	vertical displacement of soil element
$\vec{v}$	normal vector to the intergranular contact plane
w	pile head displacement
w_P	pile head displacement at peak resistance
z	vertical distance from sample surface to soil element
α	inclination of minor principal strain E_2
Φ_{CS}^{DS}	direct shear critical-state friction angle
ξ	angle between the displacement vectors and the horizontal

Manuscript received 7 December 2018; first decision 12 February 2019; accepted 3 March 2019.

*Univ. Grenoble Alpes, CNRS, Grenoble INP, 3SR, F-38000, Grenoble, France.
†Lyles School of Civil Engineering, Purdue University, West Lafayette, IN, USA.
‡Universidad del Norte, Barranquilla, Colombia.

INTRODUCTION

Various experimental studies of the loading response of non-displacement piles in sand in the field and in the laboratory have shown that the shaft capacity of fresh non-displacement piles is similar for tensile and compressive loading (Chen & Kulhawy, 2002; Kulhawy, 2004; Le Kouby *et al.*, 2013; Galvis-Castro *et al.*, 2018b). According to Galvis-Castro *et al.* (2018b), the negligible effect of loading direction on the shaft resistance could be attributed to the installation method, which does not preload the soil in any way.

In an experimental study on displacement piles, Galvis-Castro *et al.* (2018a) showed that, in compressive loading, the induced principal strains have approximately the same direction as after monotonic jacking installation. In contrast, in tensile loading the principal strains rotate by approximately 90° with respect to their original directions, observed after pile installation. A hypothesis that can be made is that soil fabric evolves during tensile loading in a way consistent with the new direction of the most compressive strain. The fabric of a cohesionless granular soil represents the spatial arrangement of the particles and associated voids, including (*a*) the orientation of individual particle, (*b*) the position of the particle and its relationship to other particles (i.e. intergranular contacts) and (*c*) the orientation of voids in between the particles (Oda, 1972; Oda *et al.*, 1985).

A number of numerical studies showed the ability of discrete element modelling (DEM) to follow the evolution of contact forces networks at the sand–pile interface during pile installation (Lobo-Guerrero & Vallejo, 2005; McDowell *et al.*, 2012; Butlanska *et al.*, 2014; Ciantia *et al.*, 2016). The determination of mathematical representations of soil fabric entities is fairly straightforward with DEM, but the results are often limited to two-dimensional (2D) or idealised particles. Experimentally, advanced imaging techniques, such as X-ray tomography, offer new possibilities to achieve grain-scale measurements during loading (e.g. Hall *et al*., 2010; Saadatfar *et al*., 2012; Andò *et al*., 2013; Druckrey *et al*., 2018). X-ray tomography was successfully used to quantitatively analyse deformation mechanisms during pile installation in sand, including volumetric behaviour, individual grain displacements and local porosity changes (Silva & Combe, 2014; Doreau-Malioche *et al*., 2018). However, the authors are not aware of any equivalent experimental study of intergranular contacts at the sand–pile interface.

This paper describes an innovative experimental approach, based on 2D digital image correlation (DIC) and X-ray tomography, to investigate the micro-scale mechanisms driving the macroscopic response of non-displacement piles during compressive and tensile loadings. DIC is used to obtain the displacement field and the direction of principal strains during loading. After loading, samples are recovered at the interface and imaged by X-ray tomography allowing a post-mortem study of intergranular contacts.

MATERIALS AND EXPERIMENTAL SET-UP

Model pile tests

Model pile tests were performed in a half-cylindrical calibration chamber located at the Bowen Laboratory at Purdue University. The front wall of the chamber contains three observation windows that allow capturing images during a test. Figure 1 shows the experimental set-up for model pile testing. Further details of the calibration chamber and other components of the equipment are presented in Arshad *et al*. (2014).

The soil used for this study is silica sand, known as Ohio Gold Frac sand. The index properties and the values of the roundness and sphericity parameters are summarised in Table 1. The direct shear critical-state friction angle Φ_{CS}^{DS} of the sand is equal to 32·0° (Han *et al*., 2018). The model pile used is a half-circular, closed-ended pile with a flat base (diameter $B = 31{\cdot}75$ mm). The base of the pile is instrumented with a miniature load cell of 10 kN capacity. The top load, on the head of the model pile, is measured using a tension–compression load cell with a capacity of 20 kN. The shaft load carried by the pile during load testing is computed as the difference between the top and base load. Another aspect to be considered when using model piles to study prototype piles is the normalised surface roughness R_n (Garnier *et al*., 2007). For these experiments, the roughness parameters R_{max} and R_n, as defined by Tovar-Valencia *et al*. (2018), are equal to 81·14 μm and 0·131, respectively. This relatively rough pile surface produces, during pile loading, the formation of a shear band inside the soil mass. From direct shear tests, the interface critical-state friction angle for the sand–pile interface δ_c is 28·4°. The ratio of the chamber to the pile diameter and the ratio of the pile diameter to the mean particle size are, 52 and 51·2, respectively. Details of the boundary and scale effects can be found in Galvis-Castro *et al*. (2018a). In any case, chamber boundary effects on the test results are expected to be negligible.

Two tests were performed in the DIC calibration chamber (see Table 2). Prior to preparation of the test sample, in each test, the model pile was pre-installed in the chamber to simulate the response of non-displacement piles under laboratory conditions. The test sample was prepared according to the procedure used by Tehrani *et al*. (2016). Once the chamber was filled with the sand, a surcharge of 70 kPa was applied on top of the sample. One day later, the model pile was loaded either in tension or in compression under displacement-controlled conditions at a constant rate of 0·1 mm/s. During loading, the top and base loads were recorded, and the digital images were captured from each observation window (at a rate of 2 frames/s).

Three CMOS cameras located in front of the three observation windows (see Fig. 1) were used to take digital

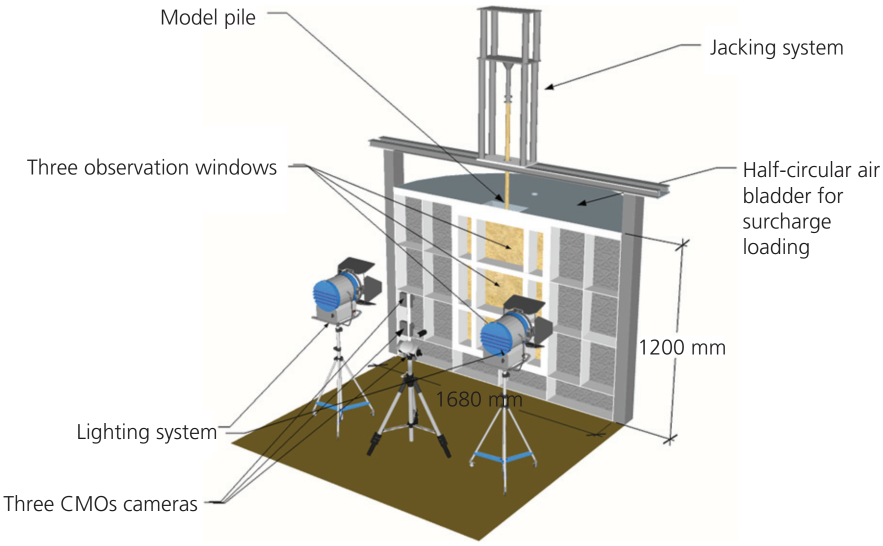

Fig. 1. Experimental equipment for model pile testing

Table 1. Index properties of Ohio Gold Frac sand (modified after Galvis-Castro *et al*., 2018a; Han *et al*., 2018)

D_{50}: mm	C_u	C_c	e_{max}	e_{min}	G_s	R^a	S^b	USCS[c]
0·62	1·44	0·94	0·81	0·59	2·65	0·43	0·83	Poorly graded

[a]Roundness (see Wadell, 1932).
[b]Sphericity (see Wadell, 1933).
[c]United Soil Classification System.

Table 2. Loading test programme

Test code	Initial relative density D_R: %	Base geometry	Initial embedment depth L_c: mm	$\lvert w_t \rvert$: mm[a]
$C(f)–D_R = 65\%$	65	Flat	370	25·0
$T(f)–D_R = 69\%$	69	Flat	400	25·0

[a]Absolute value of the pile head displacement at the end of the loading. All tests are performed with a surcharge of 70 kPa at the top of the sample, 'wished in place' and with the same surface roughness ($R_n = 0·131$).

pictures during loading. The commercial software VIC-2D (Correlated Solutions, 2009) is used to analyse the digital images captured in these experiments based on the DIC technique. The correlation algorithm used in VIC-2D is the sum-of-squared-differences (SSD) (Pan *et al*., 2009; Sutton *et al*., 2009; Take, 2015). This method is based on minimisation of the difference in grey-level intensity between a subset of a reference image and the corresponding displaced and deformed subset of the deformed image. The sub-pixel accuracy in VIC-2D is achieved interpolating the grey levels, representing the discrete grey values as a continuous 8-tap spline (Correlated Solutions, 2009). The subset – that is, the set of pixels to be tracked across images, was selected to be a square area of 25 × 25 pixels; this is approximately equal to $7D_{50}$ by $7D_{50}$. Details of DIC fundamentals and camera calibration can be found in Pan *et al*. (2009) and Arshad *et al*. (2014).

Sample recovery at sand–pile interface

The first step in the retrieval of samples for X-ray computed tomography imaging is to remove the surcharge after the load test is over. A series of turn-buckles placed between the pile and the opposite wall of the chamber keeps the model pile inside the chamber in its final position at the end of the test during surcharge removal. Once the model pile is supported, excavation of an upper layer of sand of 150 mm thickness is followed by impregnation with epoxy resin Epotek 301 (Epoxy Technology, Billerica, Massachusetts), which has low viscosity and exhibits low shrinkage during curing. After 24 h, which corresponds to the curing time required for the resin to reach its maximum hardness, the calibration chamber was emptied. The sand sample, already hardened, and the model pile were then removed from the chamber. Finally, the two sand samples recovered from each model pile test, both at a depth of 165 mm (i.e. 5·2 B), were shipped to the Laboratoire 3SR, in Grenoble, France for the X-ray scanner analysis.

X-RAY IMAGING AND CONTACT DETECTION

X-ray scans were recorded inside the X-ray scanner of Laboratoire 3SR (see Viggiani *et al*., 2015) using two different acquisition modes: *global* tomography and *local* tomography. In global tomography, the field of view contains the whole sample with a voxel size of 50 μm (i.e. there are about 10 pixels across a grain diameter). However, grain-scale measurements such as intergranular contacts require relatively high-resolution images to resolve individual grains. Thus, a trade-off has been made between the resolution and the size of the field of view: in local tomography, the field of view is reduced and contains fewer grains, which allows a voxel size of 14 μm (i.e. there are about 35 pixels across a grain diameter). A three-dimensional (3D) rendering obtained in each configuration for the tensile test is shown in Fig. 2.

In Fig. 3(a), three different phases can be observed in the grey-scale image subset obtained in local tomography: sand grains (high grey level), pores (low grey level) and resin (intermediate grey level). In order to extract the sand grains, the grey-scale images were binarised using Otsu's method (Otsu, 1979) – that is, a threshold was selected such that voxels with a grey level above this threshold are considered to be within the grain phase and those below this threshold within the 'void + resin' phase (see Fig. 3(b)). The sand grains in the binary images were then separated and were given a unique label using a 3D watershed algorithm. A number of grains can be over-segmented – that is, split into several smaller particles. This is likely due to the shape of the grains and some inclusions within the sand grains. Based on the labelled images, intergranular contacts were detected following the procedure described in Wiebicke *et al*. (2015). When the surface of contact between two particles was relatively large, the contact was treated as a segmentation error and the two particles were merged back together. Figure 3(c) shows the labelled image subset after correction of the over-segmentation.

Intergranular contacts can be directly obtained from the segmentation process. Provided that the segmentation has been conducted correctly, the voxels that have been deleted between two grains in order to separate them from each other (i.e. the watershed lines as illustrated in Fig. 3(d)) represent the contact between these two grains. A contact plane was fitted on the contact area in the labelled image and the resulting normal vector $\vec{v}$ defines the orientation of the contact. One should note that the number of intergranular

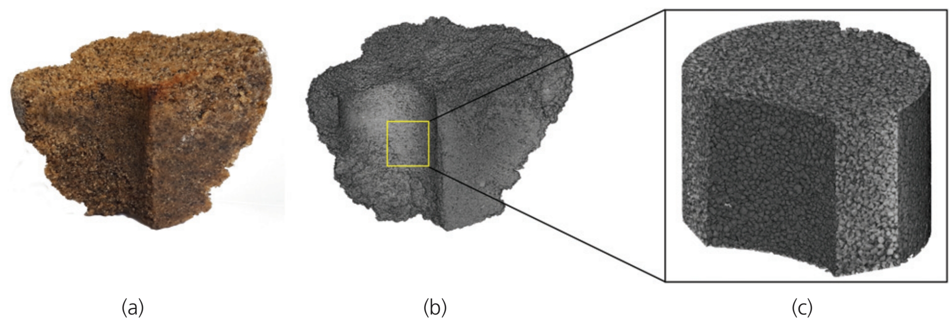

Fig. 2. (a) Sample recovered from the tensile test at sand–pile interface. 3D reconstructed volume obtained (b) in *global* tomography with a voxel size of 50 μm and (c) in *local* tomography with a voxel size of 14 μm. The square shows the reduced field of view recorded in local tomography

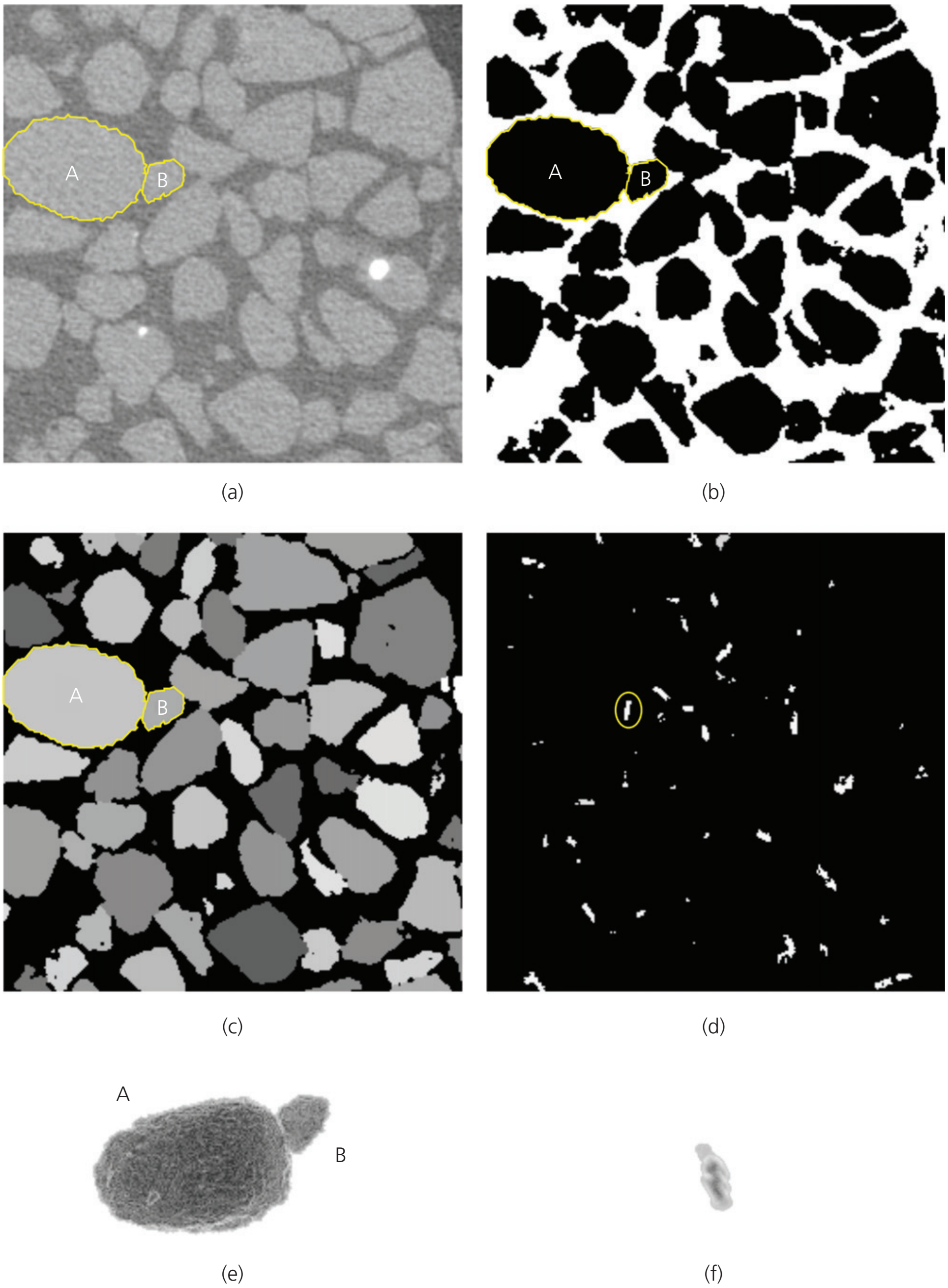

Fig. 3. (a) Grey-scale image subset showing three different phases: sand grains (high grey level), pores (low grey level) and resin (intermediate grey level). (b) Binary image after thresholding. (c) Segmented image showing two grains (A,B) in contact. (d) Watershed lines obtained from the segmentation process. The encompassed watershed line corresponds to the delimitation between grains A and B. (e) 3D rendering of the two extracted grains in contact and (f) of the corresponding contact region

contacts in a granular assembly is systematically overestimated with this technique mainly due to partial volume effect, noise and blur in the images (Wiebicke *et al*., 2017). These artefacts obviously influence significantly the measurement of contact orientation, especially in the case of complex contacts in natural sand. However, such technique allows a first qualitative analysis of contact orientations in the case of a compressive and a tensile loading of the sand-pile interface.

RESULTS

Shaft resistance

Figure 4 shows the average unit shaft resistance $q_{s,avg}$ plotted against the pile head displacement w for tensile loading (test $T(f)$–$D_R = 69\%$) and compressive loading (test $C(f)$–$D_R = 65\%$). No significant differences were found between the magnitude of the peak unit shaft resistance $|q_sP|$ for the tensile ($|q_sP| = 41{\cdot}0$ kPa) and the compressive loading ($|q_sP| = 40{\cdot}4$ kPa). In terms of pile head displacement, a slightly smaller value of displacement ($w_p = -2{\cdot}0$ mm against 3·6 mm) is required for the pile to reach the peak in shaft resistance in tensile than in compressive loading. For the compressive loading, after a pile head displacement w of 15·9 mm ($= 0{\cdot}5B$), the unit shaft resistance reaches a limit value $q_sL = 26{\cdot}6$ kPa. For the same magnitude of pile displacement ($|w| = 0{\cdot}5B$), the magnitude of the $q_{s,avg}$ for the tensile loading is equal to 30·8 kPa. At the end of pile loading, at $w = 25$ mm, $|q_{s,avg}|$ for tensile loading is comparable to $|q_{s,avg}|$ for compressive loading,

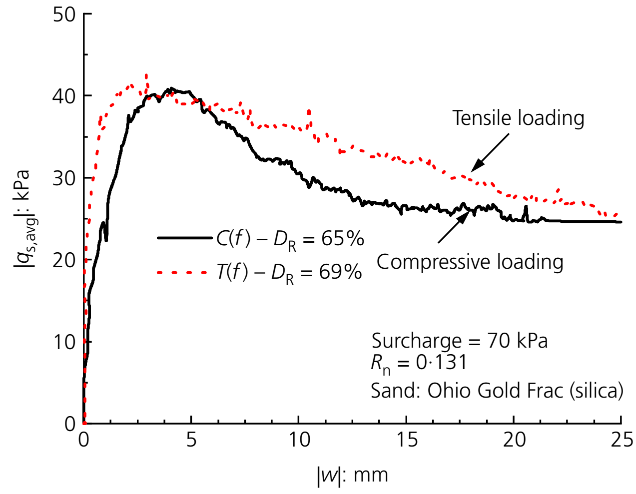

Fig. 4. Average unit shaft resistance $|q_{s,avg}|$ plotted against pile head displacement $|w|$

indicating a minimal effect of loading direction on shaft resistance of fresh non-displacement piles.

Soil displacements from 2D DIC

Figure 5 shows the soil displacement vectors, linearly scaled by the magnitude of the displacement, after $|w| = 3$ mm – near the pile displacement at which the peak in shaft resistance occurs – for compressive and tensile loading. The displacement vectors are plotted in the z/r_p against r/r_p, where z is the vertical distance from the sample surface, r is the radial distance relative to the pile axis and r_p is the radius of the model pile. For both loading directions, the magnitude of the displacement vectors decreases with increasing r/r_p; displacements tend to be greater in the compressive than in the tensile loading. The radial component of the displacement vectors indicates that soil elements move radially away from the pile shaft for both loading directions, suggesting that the soil tends to dilate. Using X-ray radiography and DIC technique, Kabla & Senden (2009) observed a reduction on the local density in the vicinity of a wall that moves upward in a container filled with monodisperse acrylic spheres, which is consistent with the DIC results from the half-cylindrical calibration chamber.

The displacement vectors show that soil elements near the pile shaft move in a steep trajectory, with the vertical component of the displacement pointing in the same direction as that of the loading.

The inclination of the displacement vectors can be expressed by the angle ξ between the displacement vectors and the horizontal (measured counter-clockwise on the right side of the pile). The results show that ξ is maximum close to the pile shaft for both, tensile loading (between $8 < z/r_p < 11$ and at $r/r_p = 1{\cdot}2$, $\xi = 69{\cdot}3°$ on average) and compressive loading (between $8 < z/r_p < 11$ and at $r/r_p = 1{\cdot}2$, $\xi = -72{\cdot}1°$ on average). Away from the pile shaft, the inclination of the displacement vectors is much less: at $r/r_p = 3$, $\xi = 40°$ for tensile loading and $\xi = -60°$ for compressive loading.

Inclination of principal strains

Figure 6 shows the contours of the inclination α of minor principal strain E_2 (i.e. the largest compressive principal strain in the r–z plane) of the Green-St. Venant strain tensor around the shaft of the model pile ($1{\cdot}1 < r/r_p < 6$ and $8 < z/r_p < 11$) after a $|w|$ of 20 mm for the tensile and compressive loading. At $|w|$ = 20 mm, the directions of the minor principal strain E_2 with respect to the horizontal close to the pile shaft (at $r/r_p = 1{\cdot}2$) are $-47{\cdot}0°$ in compressive loading and $+46{\cdot}8°$ in tensile loading, but this angle decreases for soil elements located further away radially.

Figure 7 shows the inclination α of minor principal strain E_2 plotted against the absolute value $|w|$ of the pile head displacement of two soil elements located at different initial r/r_p positions (1·3 and 2·0) but all at the same depth $z = 9r_p$. During the compressive loading, the direction α of the principal strain E_2 takes an approximately constant value of $-45{\cdot}4°$ after $|w| = 3{\cdot}0$ mm until the end of pile loading. The inclination α of the minor principal strain is also constant for tensile loading at $|w| > 3{\cdot}0$ mm but with a value of 48·4°, which shows an offset of nearly 90° to the value of α for compressive loading.

Intergranular contacts

The orientation of an intergranular contact is defined as the angle θ between $\vec{v}$ (normal to the contact plane) and the vertical axis, which also represents the pile axis denoted $\vec{z}$.

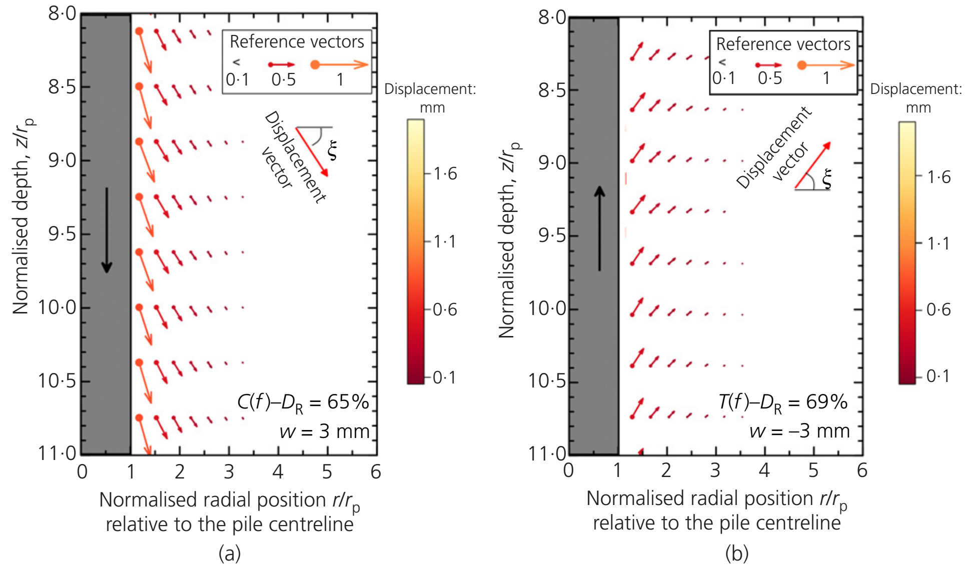

Fig. 5. Displacement vectors after an absolute value of pile head displacement of 3 mm for (a) compressive loading (test $C(f)$–D_R = 65%) and (b) tensile loading (test $T(f)$–D_R = 69%)

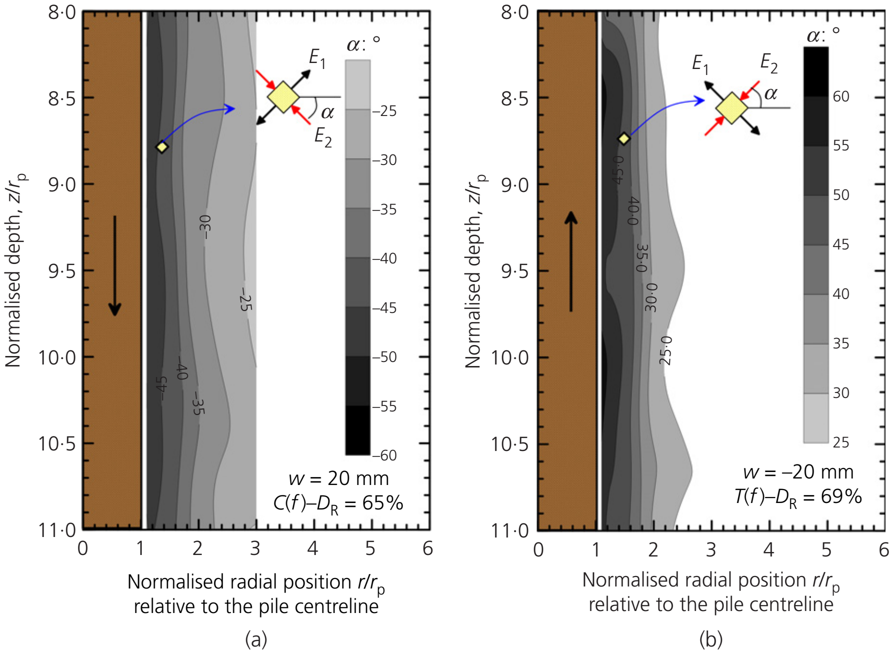

Fig. 6. Contours of the inclination α of minor principal strain E_2 (largest compressive strain in r–z plane) for the (a) compressive loading (test $C(f)$–$D_R = 65\%$) and (b) tensile loading (test $T(f)$–$D_R = 69\%$)

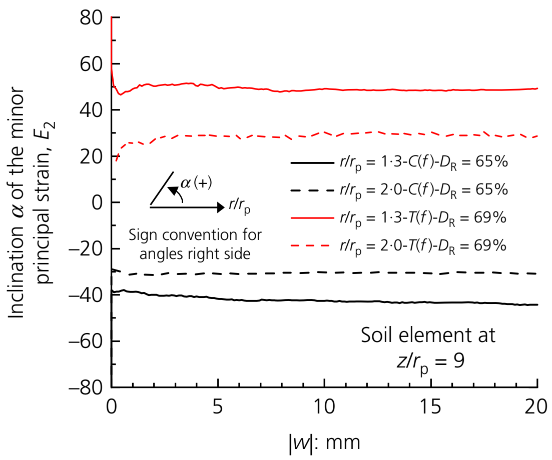

Fig. 7. Inclination α of minor principal strain E_2 plotted against absolute value $|w|$ of the pile head displacement of two soil elements for the (a) compressive loading (test $C(f)$–$D_R = 65\%$) and (b) tensile loading (test $T(f)$–$D_R = 69\%$)

As a result of the axisymmetry around $\vec{z}$, the distribution of the orientations can be expressed by the probability density function (PDF) of cos $(\theta) = x$, denoted $p(x)$, with $0 \leq \theta \leq \pi$. By construction, $p(x)$ is an even function, constant for an isotropic system. Such a function can be expanded in the series of Legendre polynomials, with only terms of even order, truncated after the fourth order

$$p(x) = 1 + A_1(3x^2 - 1) + A_2(35x^4 - 30x^2 + 3) \qquad (1)$$

in which the coefficients A_1 and A_2 are related to the moments of the distribution

$$A_1 = \frac{15}{4}\left(\langle x^2\rangle - \frac{1}{3}\right)$$
$$A_2 = \frac{9}{64}\left(35\langle x^4\rangle - 30\langle x^2\rangle + 3\right) \qquad (2)$$

Coefficient A_1 can be used to describe the anisotropy of the distribution as it is directly related to the difference between the second moment and its isotropic value (1/3). This method has been proposed in a number of numerical studies to analyse the intergranular contacts anisotropy in a granular assembly (e.g. Khalili *et al.*, 2017).

Intergranular contacts are studied within two subdomains obtained by revolution of a rectangular cross-section of the width, which is equal to the thickness of the shear band reported by Galvis-Castro *et al.* (2018b) – that is, $3{\cdot}5D_{50} \simeq 0{\cdot}14r_p$ and the height, which is equal to $r_p = 27D_{50}$. The first subdomain (see Fig. 8(a)) is located next to the pile shaft surface (from $r = r_p$ to $r = r_p + 3{\cdot}5D_{50}$) and the second subdomain at a distance of one radius from the pile shaft surface (from $r = 2r_p$) to $r = 2r_p + 3{\cdot}5D_{50}$. Each subdomain contains about 1000 grains and 2000 grains, respectively. For compressive loading, the mean number of contacts per grain (also called the coordination number) equals 5·1 for the subdomain from $r = r_p$ to $r = r_p + 3{\cdot}5D_{50}$ and 6·7 for the subdomain from $r = 2r_p$ to $r = 2r_p + 3{\cdot}5D_{50}$. For tensile loading, the corresponding mean coordination number equals 5·1 and 5·9. These results show that the number of contacts at the sand-pile interface tends to decrease for both tests, which is consistent with the radial dilation of the soil measured in the vicinity of the pile by Galvis-Castro *et al.* (2018b).

Figures 8(b) and 8(c) show the distribution of contact orientations for the subdomain from $r = 2r_p$ to $r = 2r_p + 3{\cdot}5D_{50}$ for compressive and tensile loading, respectively. The results indicate that Legendre polynomials expansion truncated at the order 4 (equation (1)) provides a good fit of the PDF of $|x|$ in both cases ($P(|x|) = 2p(x)$). Both tests exhibit a relatively low anisotropy of contact orientations, in particular in the case of the tensile test ($\langle x^2\rangle - (1/3) = 0{\cdot}004$). DIC results (section '*Soil displacements from 2D DIC*') showed that the largest soil displacements occur at a distance less than $2r_p$ from the pile axis. Thus, it can be assumed that the intergranular contacts outside of this region have the same orientation as in the initial state – that is, before the loading of the pile.

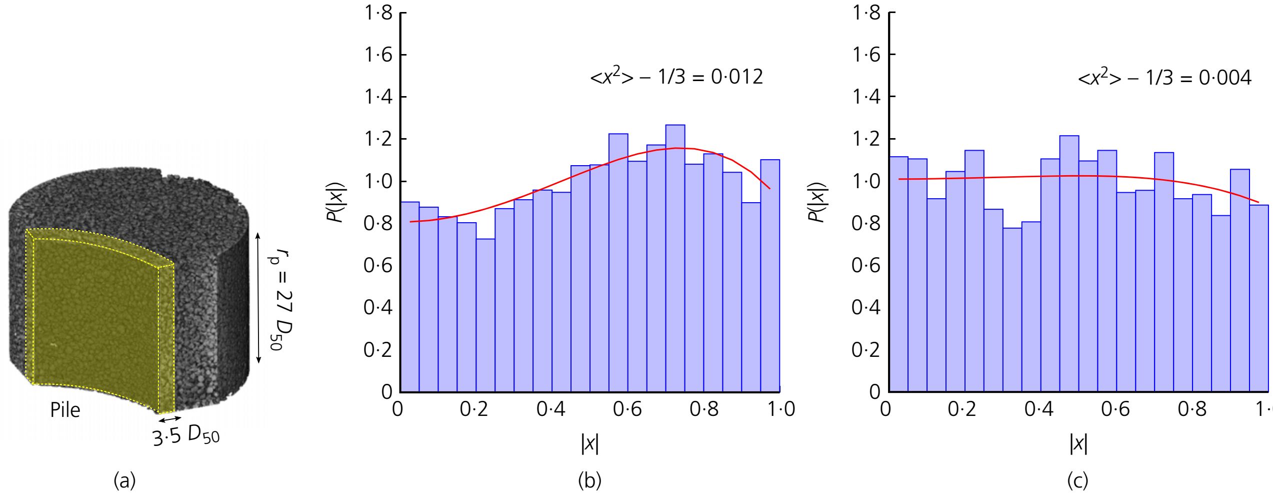

Fig. 8. (a) Schematic representation of the cross-section defining the subdomain from $r = r_p$ to $r = r_p + 3{\cdot}5D_{50}$ over which the contact orientations are studied. Distribution of contact orientations and its representation using Legendre polynomials expansion truncated at the fourth order for the subdomain from $r = 2r_p$ to $r = 2r_p + 3{\cdot}5D_{50}$: (b) after compressive loading (test $C(f)$ –D_R = 65%) and (c) after tensile loading (test $T(f)$–D_R = 69%). The quality of the Legendre polynomial fits can be estimated by the NashSutcliffe model efficiency coefficient (NSE, Nash & Sutcliffe, 1970) that ranges from $-\infty$ to 1, the latest indicates a perfect fit. (b) NSE = 0·994; (c) NSE = 0·984

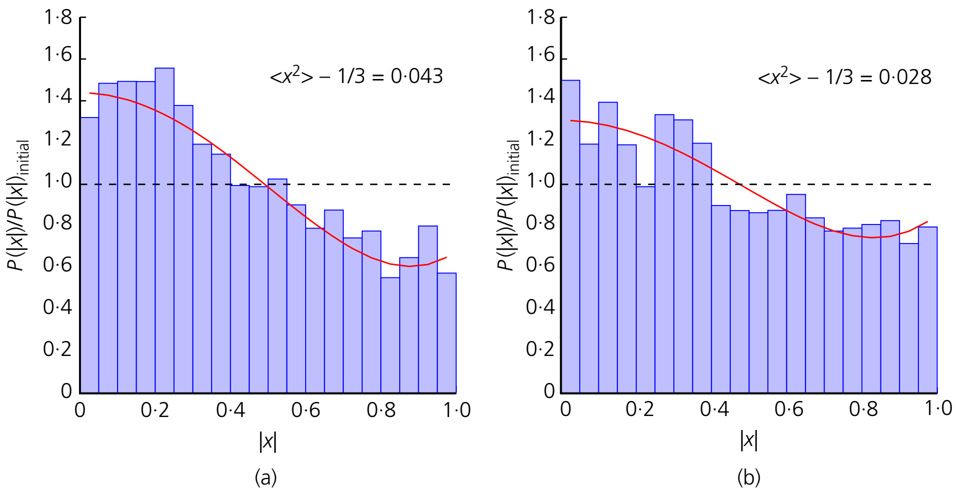

Fig. 9. Ratio $\Delta P(|x|) = P(|x|)/P(|x|)_{\text{initial}}$ defined as the ratio between the distribution of contact orientations obtained for the subdomain next to the pile shaft (from $r = r_p$ to $r = r_p + 3{\cdot}5D_{50}$) to that of the subdomain from $r = 2r_p$ to $r = 2r_p + 3{\cdot}5D_{50}$: (a) after compressive loading (test $C(f)$–D_R = 65%) and (b) after tensile loading (test $T(f)$–D_R = 69%). (a) NSE = 0·991; (b) NSE = 0·987

The ratio $\Delta P(|x|) = P(|x|)/P(|x|)_{\text{initial}}$, defined as the ratio between the distribution of contact orientations obtained for the subdomain next to the pile shaft (from $r = r_p$ to $r = r_p + 3{\cdot}5D_{50}$) to that of the subdomain from $r = 2r_p$ to $r = 2r_p + 3{\cdot}5D_{50}$ (referred to as $P(|x|)_{\text{initial}}$), for compressive and tensile loading is plotted in Figs 9(a) and 9(b), respectively. These results show that, inside the shear band, a strong anisotropy of contact orientation developed. One can observe that contacts oriented between 60° and 90° ($0 \leq |\cos\ \theta| \leq 0{\cdot}5$) are contacts that are gained ($\Delta P(|x|) > 1$), whereas, contacts with orientation θ between 0° and 60° ($0{\cdot}5 \leq |\cos\ \theta| \leq 1$) are contacts that are lost ($\Delta P(|x|) < 1$). This observation can be made for both compressive and tensile loading tests.

Oda & Konishi (1974); Matsuoka *et al.* (1988); Lanier & Combe (1995); Calvetti *et al.* (1997) observed that, during simple shear tests on granular material, the gained contacts normals concentrate towards the principal direction of compression (i.e. 45° measured with respect to the pile axis). Although results from X-ray CT analysis show that contacts orient towards 60° and 90° with respect to the pile axis (subdomain $r = r_p$ to $r = r_p + 3{\cdot}5D_{50}$), the loading of the pile induces an anisotropy of contact orientations inside the shear band. Outside the shear band – that is, $r_p \leq r \leq 2r_p$, no evolution of contact orientations was observed. The deposition of the soil around the pile, the surcharge removal at the end of the test, the soil impregnation and the drying of the resin might have had an influence in these results, and so further investigation is needed.

CONCLUSIONS

Axial loading of a pile leads to relatively large shear strains along the pile shaft; this happens even under service loads along most of the shaft for most design scenarios. Thus, understanding what happens within and around the shear band that forms next to the shaft is of interest for the development of design methods for piles, in addition to offering a variety of insights into how soil fabric might evolve on loading. In this paper, two state-of-the-art experimental methods are employed to investigate the micro-scale mechanisms driving the macroscopic response of non-displacement piles during compressive and tensile loadings. 2D DIC results show that extension (stretching) takes place in the sand surrounding the pile during both compressive and tensile loading. At the end of the loading, the directions of the minor principal strain with respect to the horizontal close to the pile shaft (at $r/r_{\mathrm{p}} = 1{\cdot}2$) reach $-47{\cdot}0°$ in compressive loading and $+46{\cdot}8°$ in tensile loading, but this angle decreases for soil elements located further away radially. Novel results obtained by means of X-ray tomography showed an evolution of fabric anisotropy in terms of intergranular contact orientations after compressive and tensile loading. Inside the shear band, where the soil has dilated to the critical state, the mean coordination number decreases and contacts are reoriented towards 60° and 90° with respect to the pile axis. A rather straightforward perspective is to combine these two experimental methods in order to link the evolution of the soil fabric to the macroscopic response of the sand-pile interface.

ACKNOWLEDGEMENTS

The authors gratefully acknowledge Pascal Charrier and Edward Andò from Laboratoire 3SR, for their contributions. Laboratoire 3SR is part of the LabEx Tec 21 (Investissements dAvenir grant agreement number ANR-11-LABX-0030).

REFERENCES

Andò, E., Hall, S., Viggiani, G. & Desrues, J. (2013). Experimental micro-mechanics of granular media studied by x-ray tomography: recent results and challenges. *Géotech. Lett.* **3**, No. 3, 142–146, https://doi.org/10.1680/geolett.13.00036.

Arshad, M. I., Tehrani, F. S., Prezzi, M. & Salgado, R. (2014). Experimental study of cone penetration in silica sand using digital image correlation. *Géotechnique* **64**, No. 7, 551–569, https://doi.org/10.1680/geot.13.P.179.

Butlanska, J., Arroyo, M., Gens, A. & OSullivan, C. (2014). Multi-scale analysis of cone penetration test (CPT) in a virtual calibration chamber. *Can. Geotech. J.* **51**, No. 1, 51–66.

Calvetti, F., Combe, G. & Lanier, J. (1997). Experimental micromechanical analysis of a 2D granular material: relation between structure evolution and loading path. *Mech. Cohesive Frict. Mater.* **2**, No. 2, 121–163.

Chen, Y. J. & Kulhawy, F. H. (2002). Evaluation of drained axial capacity for drilled shafts. *Deep foundations 2002. An international perspective on theory, design, construction, and performance* (eds M. O'Neill and F. Townsend), pp. 1200–1214. Reston, VA, USA: ASCE.

Ciantia, M. O., Arroyo, M., Butlanska, J. & Gens, A. (2016). DEM modelling of cone penetration tests in a double-porosity crushable granular material. *Comput. Geotech.* **73**, 109–127.

Correlated Solutions (2009). VIC-2D [Computer software]. Columbia, SC, USA: Correlated Solutions.

Doreau-Malioche, J., Combe, G., Viggiani, C. & Toni, J. B. (2018). Shaft friction changes for cyclically loaded displacement piles: an X-ray investigation. *Géotech. Lett.* **8**, No. 1, 66–72, https://doi.org/10.1680/jgele.17.00141.

Druckrey, A., Alshibli, K. A. & Al-Raoush, R. (2018). Discrete particle translation gradient concept to expose strain localization in sheared granular materials using 3D experimental kinematic measurements. *Géotechnique* **68**, No. 2, 162–170, https://doi.org/10.1680/jgeot.16.P.148.

Galvis-Castro, A. C., Tovar-Valencia, R. D., Salgado, R. & Prezzi, M. (2018a). Effect of loading direction on the shaft resistance of jacked piles in dense sand. *Géotechnique* **69**, No. 1, 16–28, https://doi.org/10.1680/jgeot.17.P.046.

Galvis-Castro, A. C., Tovar-Valencia, R. D., Salgado, R. & Prezzi, M. (2018b). Compressive and tensile shaft resistance of non-displacement piles in sand. *J. Geotech. Geoenviron. Engng* (under review).

Garnier, J., Gaudin, C., Springman, S. M., Culligan, P. J., Goodings, D., Konig, D., Kutter, B., Phillips, R., Randolph, M. F. & Thorel, L. (2007). Catalogue of scaling laws and similitude questions in geotechnical centrifuge modelling. *Int. J. Phys. Model. Geotech.* **7**, No. 3, 01–23, https://doi.org/10.1680/ijpmg.2007.070301.

Hall, S., Bornert, M., Desrues, J., Pannier, Y., Lenoir, N., Viggiani, G. & Bsuelle, P. (2010). Discrete and continuum experimental study of localised deformation in Hostun sand under triaxial compression using X-ray CT and 3D digital image correlation. *Géotechnique* **60**, No. 5, 315–322, https://doi.org/10.1680/geot.2010.60.5.315.

Han, F., Eshan, G., Salgado, R. & Prezzi, M. (2018). Effects of interface roughness, particle geometry, and gradation on the sand steel interface friction angle. *J. Geotech. Geoenviron. Engng* **144**, No. 12, 04018096.

Kabla, A. J. & Senden, T. J. (2009). Dilatancy in slow granular flows. *Phys. Rev. Lett.* **102**, No. 22, 228–301.

Khalili, M. H., Roux, J. N., Pereira, J. M., Brisard, S. & Bornert, M. (2017). Numerical study of one-dimensional compression of granular materials. I. Stress−strain behavior, microstructure, and irreversibility. *Phys. Rev.* **95**, No. 3, 032907, https://doi.org/10.1103/PhysRevE.95.032907.

Kulhawy, F. H. (2004). On the axial behavior of drilled foundations. *Geosupport 2004* (ed. P. Mayne), pp. 34–51. Reston, VA, USA: ASCE.

Lanier, J. & Combe, G. (1995). An experimental study of deformation in 2D-granular media. In *Proceedings of the international workshop on homogenisation, theory of migration and granular bodies* (eds E. Dembicki, J.-L. Auriault and Z. Sikora), pp. 143–149.

Le Kouby, A., Dupla, J. C., Canou, J. & Francis, R. (2013). Pile response in sand: experimental development and study. *Int. J. Phys. Model. Geotech.* **13**, No. 4, 122–137, https://doi.org/10.1680/ijpmg.13.00005.

Lobo-Guerrero, S. & Vallejo, L. E. (2005). A particle refinement method for simulating DEM of cone penetration testing in granular materials. *Géotechnique* **55**, No. 8, 617–623, https://doi.org/10.1680/geot.2005.55.8.617.

Matsuoka, H., Sakakibara, K. & Suzuki, Y. (1988). A constitutive model for granular materials evaluating principal stress rotation. In *Proc. of the U.S./Japan seminar on the micromechanics of granular materials* (eds M. Satake and J.T. Jenkins), vol. 20, pp. 287–296. Sendai-Zao, Japan: Elsevier.

McDowell, G. R., Falagush, O. & Yu, H. S. (2012). A particle refinement method for simulating DEM of cone penetration testing in granular materials. *Géotech. Lett.* **2**, No. 3, 141–147, https://doi.org/10.1680/geolett.12.00036.

Nash, J. E. & Sutcliffe, J. V. (1970). River flow forecasting through conceptual models Part I – a discussion of principles. *J. Hydrol.* **10**, No. 3, 282–290.

Oda, M. (1972). Initial fabrics and their relations to mechanical properties of granular material. *Soils Found.* **12**, No. 1, 17–36.

Oda, M. & Konishi, J. (1974). Microscopic deformation mechanism of granular material in simple shear. *Soils Found.* **14**, No. 4, 25–38.

Oda, M., Nemat-Nasser, S. & Konishi, J. (1985). Stress-induced anisotropy in granular masses. *Soils Found.* **25**, No. 3, 85–97.

Otsu, N. (1979). Threshold selection method from gray-level histograms. *IEEE Trans. Systems, Man, and Cybernet.* **9**, No. 1, 62–66.

Pan, B., Qian, K., Xie, H. & Asundi, A. (2009). Two-dimensional digital image correlation for in-plane displacement and strain measurement: a review. *Meas. Sci. Technol.* **20**, No. 6.

Saadatfar, M., Francois, N., Arad, A., Madadi, M., Cruikshank, R., Seyed Alizadeh, S., Sheppard, A., Kingston, A., Limaye, A., Senden, T. & Knackstedt, M. (2012). 3D mapping of deformation in an uncosolidated sand: a micro mechanical study. *Society of Exploration Geophysicists Annual Meeting (SEG 2012)*, pp. 1–6.

Silva, M. & Combe, G. (2014). Sand displacement field analysis during pile installation using X-ray tomography and digital image correlation. In *Proceedings of the international symposium on geomechanics from micro to macro*, Cambridge, UK (eds

K. Soga, K. Kumar, G. Biscontin and M. Kuo), pp. 1599–1603. the Netherlands: CRC Press.

Sutton, M., Orteu, J. & Schreier, H. (2009). *Image correlation for shape, motion and deformation measurements: basic concepts, theory and applications.* New York, NY, USA: Springer.

Take, W. A. (2015). Thirty-Sixth Canadian Geotechnical Colloquium: advances in visualization of geotechnical processes through digital image correlation. *Can. Geotech. J.* **52**, No. 9, 1199–1220.

Tehrani, F. S., Han, F., Salgado, R., Prezzi, M., Tovar, R. D. & Castro, A. G. (2016). Effect of surface roughness on the shaft resistance of non-displacement piles embedded in sand. *Géotechnique* **66**, No. 5, 386–400, https://doi.org/10.1680/jgeot.15.P.007.

Tovar-Valencia, R. D., Galvis-Castro, A. C., Salgado, R. & Prezzi, M. (2018). Effect of surface roughness on the shaft resistance of displacement model piles in sand. *J. Geotech. Geoenviron. Engng* **144**, No. 3, 04017120.

Viggiani, G., Andò, E., Takano, D. & Santamarina, J. C. (2015). X-ray tomography: a valuable experimental tool for revealing processes in soils. *Geotech. Test. J., ASTM* **38**, No. 1, 61–71.

Wadell, H. (1932). Volume, shape, and roundness of rock particles. *J. Geol.* **40**, No. 5, 443–451.

Wadell, H. (1933). Sphericity and roundness of rock particles. *J. Geol.* **41**, No. 3, 310–331.

Wiebicke, M., Andò, E., Viggiani, G. & Herle, I. (2015). Towards the measurement of fabric in granular materials with x-ray tomography. In *Proceedings of the 6th International Symposium on Deformation Characteristics of Geomaterials*, Buenos Aires (eds V. A. Rinaldi, M. E. Zeballos and J. J. Clariá), pp. 423–430. Buenos Aires, Argentina: IOS Press.

Wiebicke, M., Andò, E., Herle, I. & Viggiani, G. (2017). On the metrology of interparticle contacts in sand from x-ray tomography images. *Meas. Sci. Technol.* **28**, No. 12, 124007.

HOW CAN YOU CONTRIBUTE?

To discuss this paper, please submit up to 500 words to the editor at journals@ice.org.uk. Your contribution will be forwarded to the author(s) for a reply and, if considered appropriate by the editorial board, it will be published as a discussion in a future issue of the journal.